Effect of oxygen content on the sub-grain nanoindentation response in titanium affected by high temperature oxidation

Damien Texier, Quentin Sirvin, Ayyoub Dziri, Henry Proudhon, Vladislav Yastrebov, Marc Legros

▶ **To cite this version:**

Damien Texier, Quentin Sirvin, Ayyoub Dziri, Henry Proudhon, Vladislav Yastrebov, et al.. Effect of oxygen content on the sub-grain nanoindentation response in titanium affected by high temperature oxidation. Ti-2023-World Titanium Conference 2023, Jun 2023, Edinburgh, United Kingdom. hal-04167316

HAL Id: hal-04167316
https://imt-mines-albi.hal.science/hal-04167316

Submitted on 24 Jul 2023

HAL is a multi-disciplinary open access archive for the deposit and dissemination of scientific research documents, whether they are published or not. The documents may come from teaching and research institutions in France or abroad, or from public or private research centers.

L'archive ouverte pluridisciplinaire **HAL**, est destinée au dépôt et à la diffusion de documents scientifiques de niveau recherche, publiés ou non, émanant des établissements d'enseignement et de recherche français ou étrangers, des laboratoires publics ou privés.

EFFECT OF OXYGEN CONTENT ON THE SUB-GRAIN NANOINDENTATION RESPONSE IN TITANIUM AFFECTED BY HIGH TEMPERATURE OXIDATION

Damien Texier[1], Quentin Sirvin[1], Ayyoub Dziri[1], Henry Proudhon[2], Vladislav Yastrebov[2], Marc Legros[3]

1 Institut Clément Ader (ICA) – UMR CNRS 5312 ; Université de Toulouse ; CNRS, IMT Mines Albi, INSA, ISAE-SUPAERO, UPS ; Albi, France.
2 Centre des Matériaux - Mines Paris PSL; Corbeil-Essonnes, France.
2 CEMES, 29 rue Jeanne Marvig ; Toulouse, France.

Pre-oxidation tests were performed on a commercially pure titanium (CP-40) at 700 °C for 100 h under air in order to introduce a gradient of oxygen content within the metal, also called the oxygen-rich layer (ORL). The chemical profile of oxygen was measured using microprobe analyses (EPMA) on cross-sectional observations. Large but highly resolved nanoindentation maps using continuous stiffness measurement techniques were performed on the specimen cross-section to document the local mechanical response within the oxygen-rich layer (ORL) as a function of the oxygen content and the grain orientation using statistical and multi-modal analyses. The oxygen was found to greatly increase the hardness and elastic modulus in titanium and was correlated to orientation of the *c* axis of the α-Ti.

Keywords: Commercial pure titanium; oxygen embrittlement; micromechanical tensile testing; gradient of properties; mechanical behavior.

1. Introduction

Titanium alloys exhibit high specific strength at room and intermediate temperatures. This property makes them interesting candidates for structural components in aircraft applications where mass is an issue [1]. However, titanium and its alloys are sensitive to oxygen dissolution at intermediate temperature due to the high solubility and diffusion of oxygen within both the α-Ti and β-Ti phases [2]. Titanium and its alloys develop an oxygen-rich layer (ORL) beneath the external oxide [3]. The ORL is brittle and highly detrimental for the mechanical integrity of thin components [4], leading to premature cracking under tensile loading. Therefore, their use at intermediate temperatures for structural application is compromised by their oxidation resistance, and more particularly by the formation of the ORL. The ORL can extend from micrometers downto hundreds of nanometers depending on the time-temperature couple and material [5]. In addition to embrittlement, oxygen insertion modifies the mechanical properties of titanium. Oxygen addition in a low concentration (tens of percent of oxygen) can significantly improve the tensile strength of titanium [6–10] at the expense of the ductility [3,6,11]. This modification in mechanical properties is partly attributed to the increase of the critical resolved shear stress (CRSS) for the different slip systems but also the hardening exponent [6,7] and a change in deformation modes from single prismatic slip to double prismatic slip or multiple slip [12]. The Young's modulus also increases with to oxygen content [9]. Within the ORL, the oxygen content can reach 25 % at. at the metal/oxide interface and decrease down to thousands of ppm in the specimen core, *i.e.*, the nominal composition of Ti and Ti alloys. At such high oxygen content, the oxidized material is particularly brittle and a drop in mechanical strength is generally observed for Ti alloys [13] but not necessarily for commercially pure titanium due to solid solution strengthening [14]. This competition between strengthening effect and damage development leading to a drop of mechanical strength is central and complementary information at the sub-grain level are needed to better consider strain heterogeneities at the grain/sub-grain level due to oxygen insertion and gradient. A better understanding of the local mechanical response at the sub-grain level is thus needed and nano-indentation techniques are well suited to assess such local mechanical properties depending either on the local crystallographic orientation of the grain and the oxygen content. Fast nanoindentation mapping was recently used on a commercially pure titanium (CP40) to correlate hardness to the declination angle of the *c* axis and oxygen content. The multi-modal map correlation and combination aimed to demonstrate the significant increase in hardness with oxygen content but its decrease with the declination angle [15]. Hardness increase using micro-hardness experiments was also reported in the literature [9,16,17]. In addition, Magazzeni *et al.* also evidenced the increase in elastic properties with the oxygen increase but no significant relation between the declination angle and the elastic response at the sub-grain level. In the present study, the nanoindentation response of "as-received" and "pre-oxidized" CP40 Ti materials was investigated at the sub-grain level using fast continuous stiffness measurement (CSM) indentation maps. Assessing the local mechanical behavior at the sub-grain level and at the sub-ORL level is important to better understand the heterogeneous and anisotropic mechanical response of Ti as a function of the grain orientation and the local oxygen content.

2. Material and experiments

2.1. *Material*

A 1.8 mm-thick sheet of commercially pure titanium (CP40) was provided by "All Metal Services" with a nominal composition of Ti-0.14%O-0.07%Fe-0.0%N-0.0%C (weight %). The material was constituted of α-phase equiaxed grains with some iron silicides located at the grain boundaries. The initial microstructure had an average grain size of 15 µm. Based on the initial texture of the CP40 sheet, EBSD analyses were performed on the as-received material in order to select a plane with the less pronounced texture along the further indentation direction. The specimen was first cut parallel to the short transverse direction (STD)- rolling direction (RD) plane then mounted in a cold epoxy resin. The mounted sample was polished down to a 1 µm diamond paste finish, then a mechanochemical polishing using colloidal silica during 40 minutes. EBSD maps were acquired using a JEOL JSM 7100F scanning electron microscope equipped with a CMOS Symmetry S2 EBSD detector (Oxford Instruments). Inverse pole figure maps in regard to the short transverse direction (STD), the rolling direction (RD), and the long transverse direction (LTD) are depicted in Figure 1. Based on this preliminary analysis, indentation along the LTD is preferred to screen a larger panel of grain orientation. This mounted sample was used for nanoindentation, and another sample was prepared to evaluate the effect of the oxygen content on the sub-grain nanoindentation response. Geometrical constraints to test the specimen along the LTD direction for nanoindentation lead us expose the LTP-RD face for oxidation and establish a gradient of oxygen along the STD. Before oxidation, the sample was polished down to a P4000 surface finish using a precision jig to ensure a good control of the sample parallelism [18]. The sample was cleaned in acetone then in ethanol in an ultrasonic bath during 15 minutes each. A Nabertherm C290 furnace with static atmosphere, *i.e.* no air stirring, was used for the 700 °C – 100 h pre-oxidation treatment. The sample was positioned onto an alumina plate with its side of interest facing the air, and was introduced in the hot furnace. After oxidation, the specimen was cut then mounted in a cold epoxy resin and was prepared as for EBSD analyses.

2.2. *Nanoindentation tests*

Nanoindentation tests were performed on a NMT04 nanoindentor (*Femtotools® AG*) equipped with a 20 mN MEMS sensor and a Berkovich diamond tip. Tests were carried out under displacement control using the continuous stiffness measurement (CSM) technique. The schematic illustration of the CSM nanoindentation test showing the sin-form signal added to the loading condition is depicted in Figure 2, as well as the typical nanoindentation force-displacement and different areas during and after unloading.

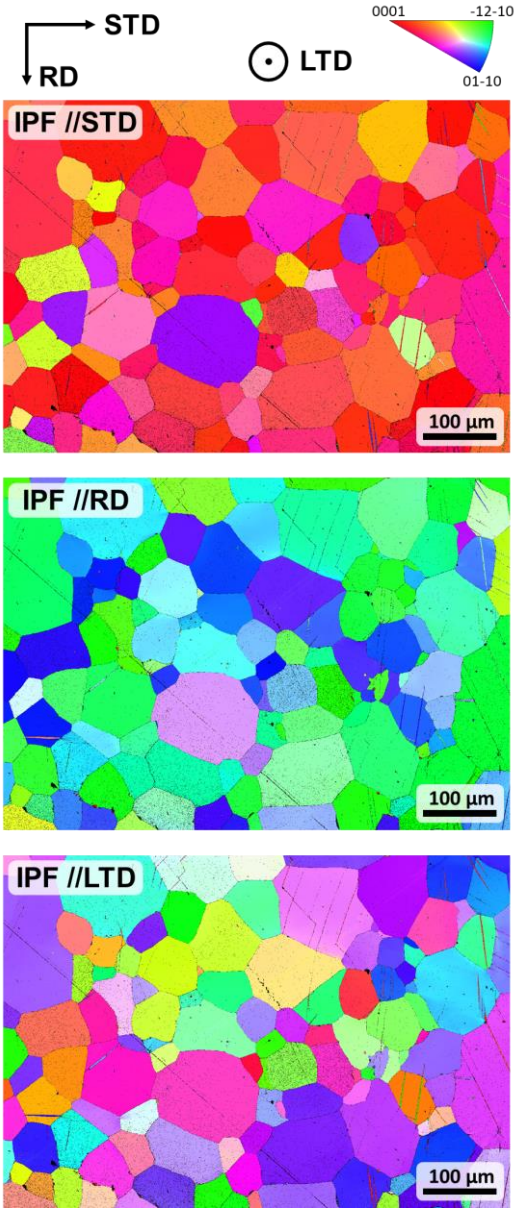

Figure 1: EBSD maps of the as received material represented as inverse pole figure in regard to the short transverse direction (STD), the rolling direction (RD) and the long transverse direction (LTD).

For information, the calculation of the reduced modulus E_r, the hardness H, and the contact depth h_c are as follows: $E_r = S\frac{\sqrt{\pi}}{2\sqrt{A}}$, with S, the system stiffness $S = \frac{dP}{dh}$ and A, the contact area to be identified during the calibration on the fused silica.

$$H = \frac{P_{max}}{A} \text{ and } h_c = h_{max} - \varepsilon\frac{P_{max}}{S}$$

The calibration consists of (1) an evaluation then correction of the frame compliance at different locations

of the in-plane motorized stage and (2) a measurement of the contact area as a function of the contact depth. The frame stiffness and tip calibrations were conducted on a standard sample made of fused silica in order to determine the contact area function as a function of the contact depth using CSM conditions. The calibration curves are shown in Figure 3. Both the reduced modulus and hardness values stabilized after a contact depth of 20 nm. For information, CSM parameters were similar for the tip calibration and the nanoindentation test performed on the sample of interest, *i.e.*, a CSM frequency of 200 Hz, an amplitude of 5 nm in a displacement control mode.

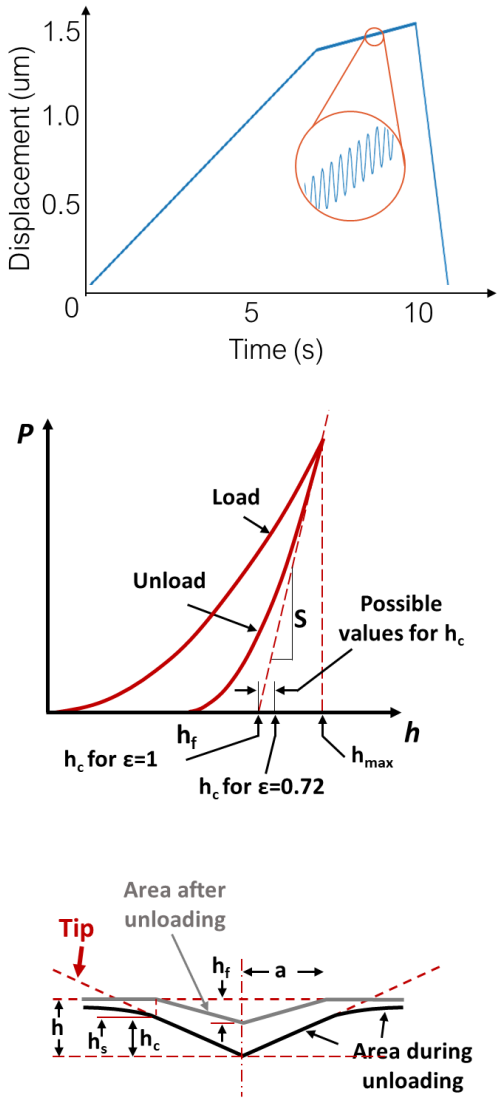

Figure 2: Illustration of the CSM nanoindentation test showing the sin-form signal added to the loading condition. Schematic illustration of the typical nanoindentation force-displacement curve and the different definition of the contact during and after unloading.

After the tip calibration, CSM nanoindentation on materials of interest were performed. Nanoindentation tests were conducted on the as-received material and on the pre-oxidized material with two different spatial measurement grids. As for the calibration, CSM nanoindentation was performed using the displacement control mode to have similar contact depth regardless of the material properties (hardness and elastic modulus). This point is particularly important due to the significant effect of oxygen insertion within Ti on the local mechanical response.

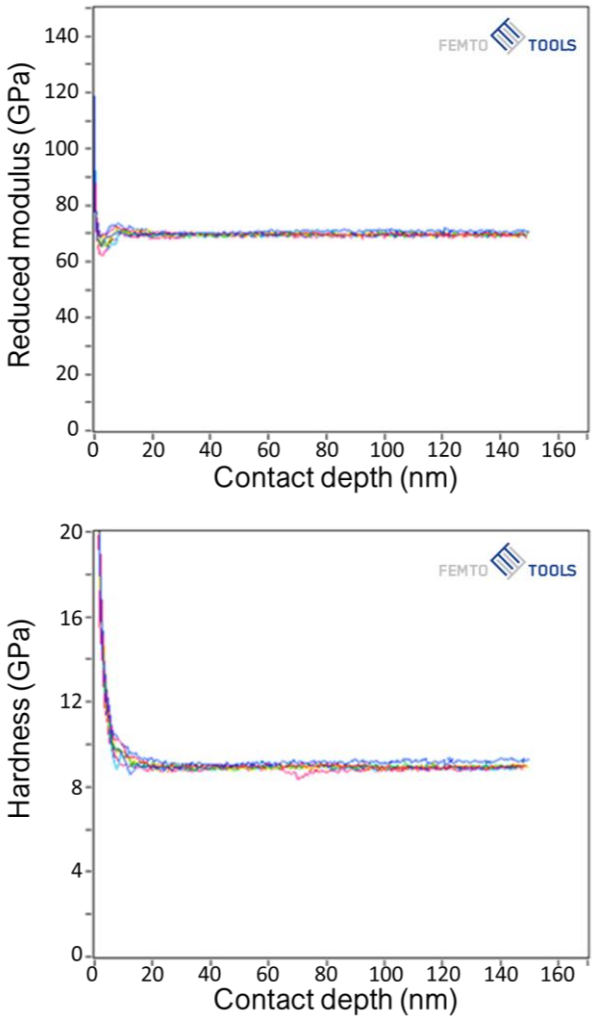

Figure 3; Calibration curves (reduced modulus and hardness as a function of the contact depth) on a fused silica standard sample

On the as-received material, the measurement grid was of 2.5 µm and the maximal contact depth was of 120 nm for a measurement grid of 400 × 240 indents. The approach speed was of 0.24 µm.s^{-1}, a load rate of 0.12 µm.s^{-1}, and a fast retractation since both the reduced modulus and the hardness were continuously measured during the loading sequence. For the large nanoindentation field on the pre-oxidized specimen,

similar nanoindentation parameters were used for a measurement grid of 1100 × 100 indents (8 % of the indents being in the resin for positioning purpose). For the higher resolution nanoindentation map on the pre-oxidized specimen, the measurement grid was of 0.8 µm and the maximal contact depth was of 50 nm for a measurement grid of 470 × 190 indents. The approach speed was of 0.1 µm.s^{-1}, a load rate of 0.025 µm.s^{-1}, and a fast retractation. Each nanoindentation maps last about 10 days.

2.3. EPMA analysis

A Cameca SXFiveFE microprobe was used for the quantitative chemical analysis of the oxygen profile after oxidation (Electron micro probe analyzer (EPMA)). Oxygen profiles on Ti and Ti alloys are difficult to obtain due to self-contamination of the specimen with the native thin TiO_2 oxide instantaneously developing after surface preparation. A particular attention was paid on the specimen preparation to limit edge blunting and surface contamination. Natural standards were used to quantitatively obtain the oxygen content difference within the ORL relative to the oxygen content within the non-affected material by spectrum subtraction to remove the signal from the native superficial oxide.

3. Results and discussion

3.1. Nanoindentation on the as-received material

The EBSD maps and nanoindentation maps of the as-received CP40 Ti material are shown in Figure 4. As aforementioned, the specimen orientation was purposely chosen to have a large panel of grain orientations to be tested using nanoindentation. Both the reduced modulus and the hardness maps were capable to depict the anisotropic response of the material at the grain scale. While maps are slightly noisy, anisotropic properties at the grain level is evidenced, making this technique capable to extract local mechanical properties, such as very narrow twins present in the material. During the CSM measurement, some stress drops were observed due to plastic activity and altered the fitting of the curves to extract the reduced modulus and hardness. Therefore, scatter within a grain can be partly explained by the number of stress-drop occurring in the fitted part of the $E_r = f(h_c)$ and $H = f(h_c)$. A 15% variation in reduced elastic properties was found between the softest and strongest crystallographic directions, [01-10] and [0001], respectively. Similar observations were found for the hardness property, with [01-10] and [-12-10] being the lowest hardness properties and [0001] being the harder ones. A factor 2 is terms of hardness value was found between the lowest hardness and highest hardness. The hardness results confirm Magazzeni *et al.* work [15]. Similar analyses using the declination angle formed between the c axis of each grain and the loading direction will be investigated for both the reduced and hardness properties. This first-order approach is interesting but does not take into account the multi-axiality of the loading inherent to the nanoindentation test. Therefore, numerical simulations of the nanoindentation test will be conducted to better link the measured reduced modulus and hardness properties as a function of the crystal orientation.

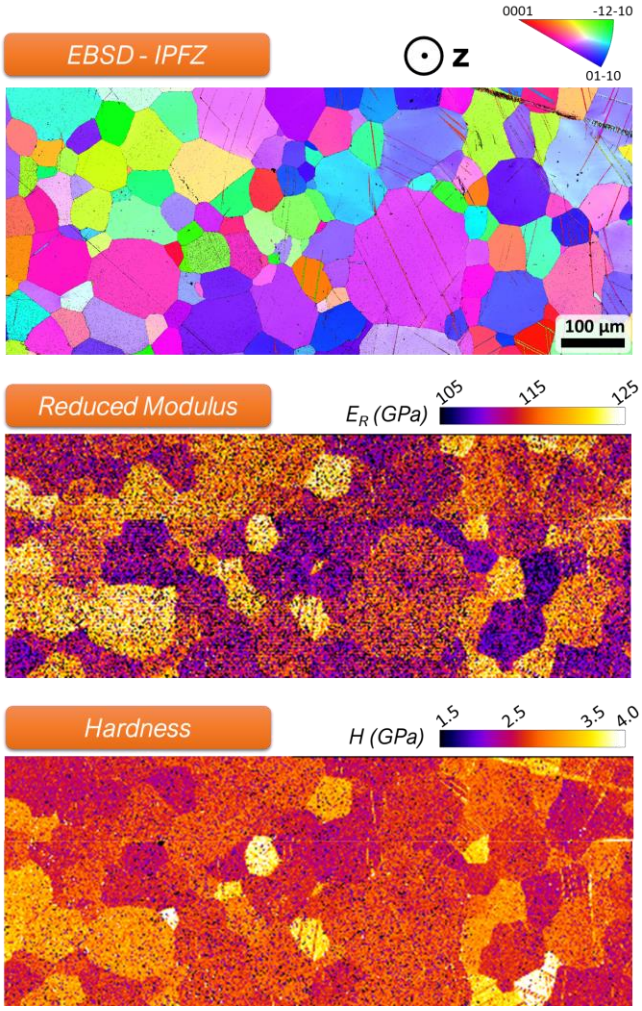

Figure 4: EBSD and nanoindentation maps for the as-received CP40 Ti material

3.2. Chemical analysis of the oxygen profile

EPMA analysis allows to quantitatively measure the element composition on the cross-section of the pre-oxidized specimen at 700 °C for 100 h (atomic %). For each analysis, four profiles were performed (Figure 5). Due to passivation of titanium at room temperature, the O content was measured relative to a reference state, *i.e.* the

non-oxidation affected material, by spectrum subtraction of O. The oxygen content at the metal oxide interface was nearly of 20% at. and gradually decrease in depth. Oxygen profiles were fitted and the extension of the ORL was considered as the depth at a difference of oxygen content of 0.5% at. more than oxygen concentration of the non-affected material. The ORL extension was found of 45 µm for an oxidation at 700 °C for 100 h.

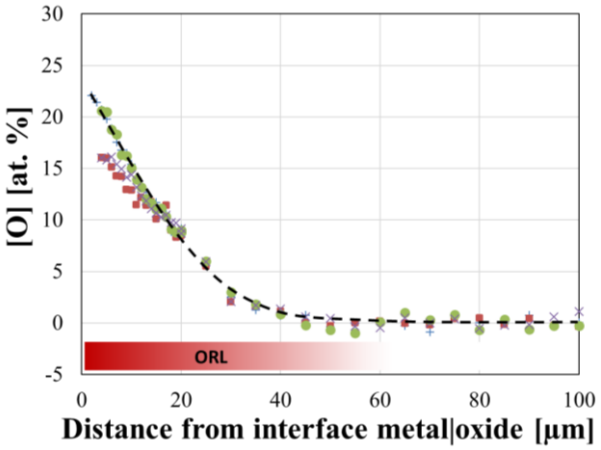

Figure 5: Oxygen profile obtained using EPMA analysis for the sample oxidized at 700 °C for 100 h

3.3. Nanoindentation on the pre-oxidized material

The EBSD maps and nanoindentation maps of the pre-oxidized CP40 Ti material are shown in Figure 6. As for the as-received material, the anisotropic response of the material at the grain level is clearly depicted on both the reduced modulus and hardness maps. Oxygen was found to significantly increase the reduced modulus and hardness properties by a factor 1.8 and 4.5, respectively. The concomitant effect of the oxygen and grain orientation onto the reduced modulus and hardness properties is observed on the present results. Some grains at the surface present a lower stiffness compared to the adjacent grain in depth due to crystallographic effect being stronger than the oxygen effect on the reduced modulus properties. This case was less encountered for the hardness properties due to the significant variation of hardness properties with oxygen insertion. Further analyses will be conducted to better dissociate the effect of the grain orientation and oxygen content on both the reduced modulus and hardness properties. In comparison with Magazzeni *et al.* [15], similar effect of the oxygen insertion was observed for the hardness properties but was not presented for the elastic properties. The anisotropic response within individual grain is better depicted in the present results. In addition, nanoindentation tests at 50 nm depth are less noisy compared to the ones at 120 nm due to a fewer stress drop events.

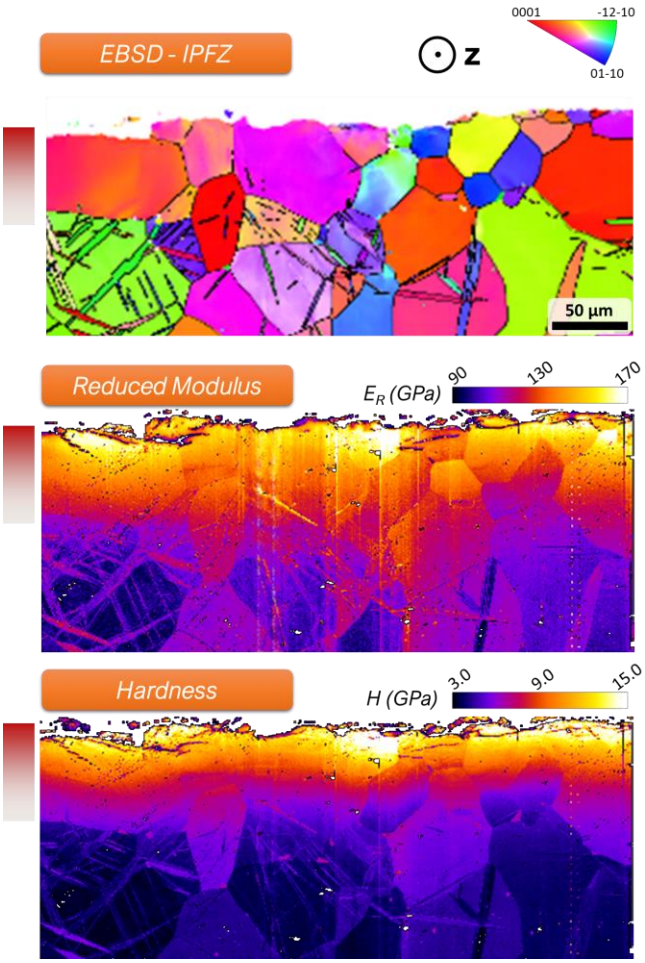

Figure 6: BSD and high resolution nanoindentation maps across the O gradient for the CP40 Ti material oxidized at 700 °C for 100 h

4. Conclusions

Large nanoindentation maps were performed to assess the local mechanical response of a large number of grains with a resolution compatible with the grain size and extension of the ORL. The anisotropy of the elastic and hardness properties related to grain orientations is highlighted thanks to CSM nanoindentation testing. The oxygen dissolved within Ti modifies both the elastic and hardness properties, leading to an increase of reduced modulus and hardness with the oxygen content. The nanoindentation technique is capable to detect twins as thin as 1 µm, related to pre-deformation during tensile loading. The following step will be to decorrelate the effects of oxygen and grain orientation on the mechanical properties, *i.e.*, elastic and hardness properties using registered CSM nanoindentation, EBSD and EPMA/EDS maps. Numerical simulations using crystal plasticity finite element methods will be further conducted to first study the effect of crystal orientation on the elastic and hardness responses of the A.R. material. The effect of the local oxygen content on the mechanical response will also be investigated.

5. Acknowledgements

This research was funded, in whole or in part, by The European Research Council, project HT-S_4DefOx - Grant number 948007]. A CC-BY public copyright license has been applied by the authors to the present document and will be applied to all subsequent versions up to the Author Accepted Manuscript arising from this submission, in accordance with the grant's open access conditions.

6. References

[1] M. Peters, J. Kumpfert, C.H. Ward, C. Leyens, Adv. Eng. Mater. 5 (2003) 419–427.

[2] J.L. Murray, H.A. Wriedt, J. Phase Equilibria 8 (1987) 148–165.

[3] W.L. Finlay, J.A. Snyder, JOM 2 (1950) 277–286.

[4] D. Texier, Q. Sirvin, V. Velay, M. Salem, D. Monceau, B. Mazères, E. Andrieu, R. Roumiguier, B. Dod, MATEC Web Conf. 321 (2020) 06004.

[5] N. Vaché, D. Monceau, Oxid. Met. 93 (2020) 215–227.

[6] G. Baur, P. Lehr, J. Less-Common Met. 69 (1980) 203–218.

[7] B. Barkia, V. Doquet, J.P. Couzinié, I. Guillot, E. Héripré, Mater. Sci. Eng. A 636 (2015) 91–102.

[8] J.-P. Couzinie, B. Barkia, V. Doquet, I. Guillot, in: 2012 Int. Hydrog. Conf., Jakson Lake (USA), 2014, pp. 411–419.

[9] F.B. Vicente, D.R.N. Correa, T.A.G. Donato, V.E. Arana-Chavez, M.A.R. Buzalaf, C.R. Grandini, Materials (Basel). 7 (2014) 542–553.

[10] M.C. Brandes, M. Baughman, M.J. Mills, J.C. Williams, Mater. Sci. Eng. A 551 (2012) 13–18.

[11] M. Yan, W. Xu, M.S. Dargusch, H.P. Tang, M. Brandt, M. Qian, Powder Metall. 57 (2014) 251–257.

[12] J.Q. Ren, Q. Wang, X.F. Lu, W.F. Liu, P.L. Zhang, X.B. Zhang, Mater. Sci. Eng. A 731 (2018) 530–538.

[13] D. Texier, Q. Sirvin, V. Velay, M. Salem, D. Monceau, B. Mazères, E. Andrieu, R. Roumiguier, B.B. Dod, in: Ti2019, Nantes (France), 2020, pp. 0–4.

[14] Q. Sirvin, D. Texier, J. Genée, V. Velay, D. Monceau, B. Dod, in: Titan. 2023, Edimbourg, 2023.

[15] C.M. Magazzeni, H.M. Gardner, I. Howe, P. Gopon, J.C. Waite, D. Rugg, D.E.J. Armstrong, A.J. Wilkinson, J. Mater. Res. 36 (2021) 2235–2250.

[16] J. Baillieux, D. Poquillon, B. Malard, J. Appl. Crystallogr. 49 (2016) 175–181.

[17] H. Hornberger, C. Randow, C. Fleck, Mater. Sci. Eng. A 630 (2015) 51–57.

[18] D. Texier, D. Monceau, J.-C. Salabura, R. Mainguy, E. Andrieu, Mater. High Temp. 33 (2016) 325–337.